# 1.3 μm InAs/GaAs quantum-dot lasers with P-type, N-type, and co-doped modulation

Huiwen Deng[1,†], Jae-Seong Park[1,†], Xuezhe Yu[1], Zizhuo Liu[1], Hui Jia[1], Haotian Zeng[1], Junjie Yang[1], Shujie Pan[1], Siming Chen[1,*], Alwyn Seeds[1], Mingchu Tang[1,*], Peter Smowton[2], Huiyun Liu[1].

[1]Department of Electronic and Electrical Engineering, University College London, Torrington Place, London, WC1E 7JE, United Kingdom

[2]School of Physics and Astronomy, Cardiff University, Cardiff, CF10 3AT, United Kingdom

†These authors contributed equally to this work.

*Corresponding author: siming.chen@ucl.ac.uk; mingchu.tang@ucl.ac.uk,

Abstract

To further enhance the performance and understand the mechanism of InAs quantum dot (QD) laser under high temperature, we investigated, both theoretically and experimentally, the effects of the technique of the combination of direct n-type doping and modulation p-type doping, namely co-doping, in the active region for a wide temperature range over 165 °C. Through the comparison of co-doped, modulation p-type doped, direct n-type doped and undoped QD lasers, it is revealed that the co-doping technique provides a significantly reduced threshold current density across the whole temperature range and robust high-temperature operation. Furthermore, it is also observed that the effectiveness of co-doping in suppressing round-state quenching is comparable to that of p-doping. The improvements in the doping strategies are also revealed through the rate equation simulation of the lasers.

## 1. Introduction

Self-assembled InAs/GaAs quantum-dot (QD) lasers have attracted considerable attention because of their unique advantages of low threshold, high-temperature operation, robust tolerance to crystal defects, low linewidth enhancement factor and insensitivity to optical feedback [1-7]. Compared with conventional quantum-well lasers, indeed, extensive works have demonstrated superior static and dynamic properties of QD lasers [8-14]. Nonetheless, the performance of QD lasers is still not ideal, partly due to the thermal escape of carriers from the ground state to higher states in QD and/or barrier layer [15, 16]. Furthermore, the closely spaced states in the valence band cause the thermal broadening of holes and, hence, the asymmetry in the charge carrier distribution in QDs, reducing the radiation efficiency and gain characteristics of QD lasers [17, 18].

In order to improve the performance of QD lasers, modulation p-type Be doping (p-type doping) technique has been widely employed to compensate for the loss of holes by providing extra holes at high operating temperature, which significantly enhance the temperature stability, gain characteristics and direct modulation response of QD lasers [19-21]. It was also demonstrated that p-type doping facilitates ground-state lasing, particularly in short-cavity lasers [22, 23]. Despite various advantages of p-type doping in QD lasers, the use of p-type doping causes an increase in the threshold current of QD lasers, mainly due to the increased non-radiative recombination and internal losses [24, 25]. Alternatively, direct n-type Si doping (n-type doping) in QDs, which is capable of passivating the non-radiative recombination centres and introducing extra electrons, has also been studied recently because it provides the improved optical properties of self-assembled QDs and significantly reduces the threshold current of lasers [26-28]. For example, Lv et al. reported that using direct n-doping in QDs produced a reduced threshold current density ($J_{th}$) of 71.6 A/cm² from 167.3 A/cm² (undoped QD lasers)

and higher operating temperatures [29]. In addition, Deng et al. demonstrated that QD lasers with n-doping showed a narrowed near-field lasing spot, along with a reduced $J_{th}$ [30].

Recently, a co-doping technique, which employs both n-type doping in QDs and p-type doping in barrier layers at the same time, was proposed to further improve the performance of QD lasers by compensating for the drawback of p-type doping [31, 32]. For instance, Lv et al. [31] demonstrated that compared with the modulation p-type dope QD lasers, the co-doped QD lasers exhibited a decrease of threshold current ($I_{th}$) from 51.07 mA to 43 mA and an increase of slope efficiency from 0.18 to 0.25 W/A under pulse mode at room temperature. Moreover, the co-doped lasers showed stable lasing operation with power exceeding 20 mW at 85 °C under continuous-wave (CW) mode operation, while the p-type doped one reached power saturation at only 14.08 mW. However, the influence of co-doping on the performance of QD lasers has not been comprehensively studied yet, particularly compared with n-type direct doped (n-doped) and undoped ones, and the mechanism of the improved lasing performance of the co-doping strategy was not clearly revealed.

In this work, we demonstrated that QD lasers were feasible to work over 165°C with further high-temperature improvements through different doping strategies. In addition, we delved into the fundamental mechanisms behind QD lasers with different doping strategies based on rate equations, demonstrating that photon lifetime is vital in controlling the $J_{th}$.

## 2. Material growth and device fabrication

### 2.1 Laser structure growth

To elucidate the impact of various doping strategies on laser performance, four identical laser structures with different doping strategies of active regions were developed under optimised growth conditions. As depicted in Figure 1 (a), these laser structures were epitaxially grown on 3-inch n-type GaAs substrates by using Veeco GEN930 molecular beam epitaxy system, commencing with a 200-nm thick n-type GaAs buffer layer. This layer was followed by a sequence of 10 repetitions of alternating n-type $Al_{0.4}Ga_{0.6}As$/GaAs superlattice layers, each 2.5 nm thick. Subsequently, a 1.4 µm thick n-type $Al_{0.4}Ga_{0.6}As$ cladding layer is incorporated into the structure. This was then succeeded by a 30-nm thick, undoped $Al_{0.4}Ga_{0.6}As$ guiding layer and finished by 12 repetitions of $Al_{0.4}Ga_{0.6}As$/GaAs superlattice.
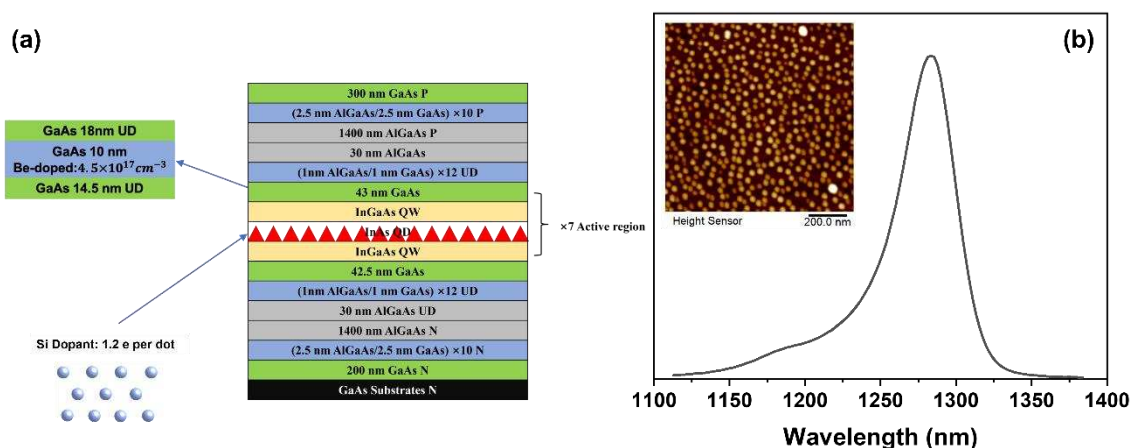


Figure 1. (a) The schematic diagram for the 1.3 µm InAs QD laser structure with the co-doping technique and (b) Typical PL result for the calibration samples with insetting the AFM result of 1 µm² area.

The active region of the laser comprised 7 stacks of InAs Dot-in-Well (DWELL) structures, while adjacent DWELL was separated by an undoped 42.5-nm GaAs spacer layer. Each stack of DWELL consisted of a 2-nm InGaAs quantum well, followed by a 2.8 ML InAs QD deposition at a nucleation

temperature of 510°C, finished by an InGaAs capping layer with a thickness of 5 nm. Optical properties were characterised by photoluminescence (PL) measurements excited by a 635-nm laser, with a peak located at 1277.0 nm and a full width at half-maximum (FWHM) of 31.58 meV, as shown in Figure 1 (b). The QD density, characterised by Atomic Force Microscopy (AFM) in the 1 $\mu m^2$ area, is estimated to be $5.2 \times 10^{10}$ cm$^{-2}$, as demonstrated in the inset of Figure 1 (b).

Above the active region, 12 repetitions of undoped $Al_{0.4}Ga_{0.6}As$/GaAs superlattice layers were placed, followed by a 30-nm thick upper undoped $Al_{0.4}Ga_{0.6}As$ guiding layer and a 1.4-µm thick upper p-type doped $Al_{0.4}Ga_{0.6}As$ cladding layer. Finally, the laser structure was finished by 10 repetitions of p-type doped $Al_{0.4}Ga_{0.6}As$ /GaAs layers followed by a 300-nm heavily p-type doped GaAs layer, serving as the p-type contact layer.

To further compare and analyse the mechanism of different doping strategies in the QD laser active region, modulation p-type doped, direct n-type doped and co-doped QD techniques were employed. In the direct n-doped QD lasers, Si dopants were introduced during the QD formation stage, achieving a doping density of 1.2 electrons per dot, which is optimised by previous research [30]. For the modulation p-type doped QD laser, a 10-nm p-type doped GaAs layer strategically embedded within the 42.5-nm GaAs spacing layer is used, while the co-doped QD laser combines these two aspects [33].

### 2.2 Laser device fabrication and characterisation

The Fabry-Pérot laser devices were fabricated with 50-µm cavity width by conventional photo-lithography and wet chemical etching. The p-type metallisation of Ti/Au (20/250-nm) was formed on top of the mesa stripe by a sputtering system. After thinning the substrate to 150-µm, the n-type electrode of Ni/AuGe/Ni/Au (10/100/10/250-nm) was deposited on the backside of a sample using a thermal evaporator. In order to form Ohmic contact, the samples were annealed at 380 °C for 1 min. Laser bars were cleaved into 1- and 2-mm cavity lengths without facet coatings and then mounted on indium-plated copper heatsinks with gold wire bonding.

### 3. Effect of co-doping on the performance of InAs/GaAs QD lasers

The fabricated broad-area lasers with 50-µm cavity width were measured under pulse mode (1 % duty cycle, 1-µs pulse width). The $J_{th}$ of co-doped, undoped, p-type doped and n-type doped QD lasers with 2-mm and 1-mm cavity length at room temperature is summarised in Table I. Figures 2 (a) and (b) show the single-side light-current (*L-I*) curves of the fabricated QD lasers with 2- and 1-mm cavity lengths at room temperature, respectively. For both cavity lengths, the co-doped QD lasers exhibit the lowest $J_{th}$ among all four different lasers regardless of the temperature. It is also observed that the $J_{th}$ of p-type doped QD lasers becomes lower than those of undoped and n-type doped QD lasers at high temperature, especially as the cavity length decreases.

Table I. The summary of the $J_{th}$ (*A/cm²*) at room temperature of undoped, n-type doped, p-type doped and co-doped lasers.

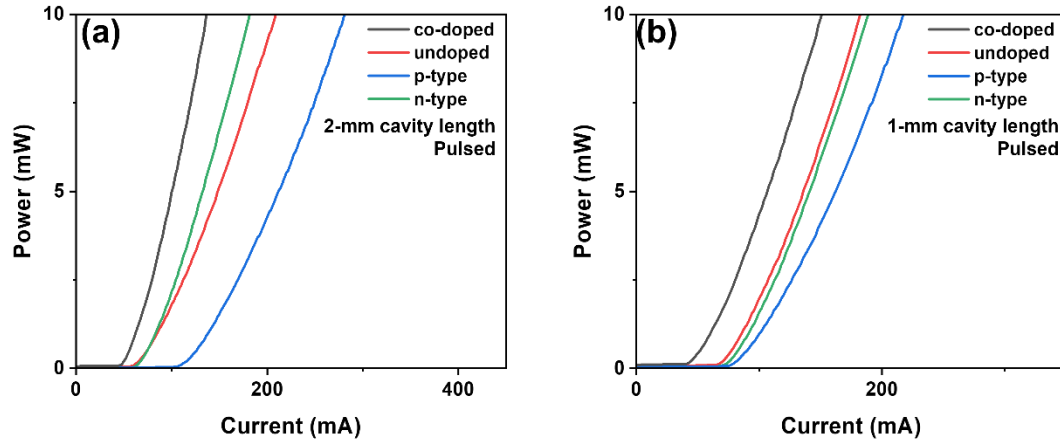| Cavity Length (mm) | 1 | 2 |
|---|---|---|
| Undoped laser | 136 | 59.12 |
| Direct n-type doped laser | 143.2 | 61.7 |
| Modulation p-type doped laser | 154.6 | 105.76 |
| Co-doped laser | 83.8 | 46.96 |

*Figure 2. Single side pulse L-I curves of QD lasers with different doping strategies at 20 ˚C (a) with 2 mm cavity length and (b) with 1 mm cavity length.*

Figure 3 (a) and (b) illustrate the $J_{th}$ trend of 2- and 1-mm cavity lengths QD laser devices on a logarithmic scale, respectively. In Figure 3 (a), it can be clearly seen that the co-doped lasers maintain the lowest $J_{th}$ in the whole temperature range. The n-type doped lasers, while initially presenting a lower $J_{th}$ than undoped and p-type doped lasers, eventually exceed that of p-type doped lasers. At the same time, 1-mm cavity length devices show a similar $J_{th}$ trend to 2-mm cavity length, as shown in Figure 3 (b). However, the $J_{th}$ of n-type doped QD lasers exceeds more rapidly than that of p-type doped lasers within a low-temperature range in a shorter cavity, and even the undoped QD laser shows similar $J_{th}$ to that of n-type doped QD lasers at a high-temperature range. The characteristic temperature ($T_0$) was calculated based on the temperature-dependent $J_{th}$ results. The p-type doped QD lasers produce the highest $T_0$, achieving 190.5 K and 86 K in the temperature range of 20 – 70 °C and above 70 °C, respectively. In comparison both the co-doped and n-type doped methods show improvements over reference undoped laser's $T_0$ of 67.1 K in the temperature range of 20 – 70 °C, reaching 109.2 K and 77 K, respectively. Furthermore, in the higher temperature range, these methods increase the $T_0$ from 37.8 K to 56 K and 45.4 K, respectively.

To identify the lasing peak wavelength, temperature-dependent wavelength shift was measured at 1.1 × threshold current ($I_{th}$), as shown in the inset figures of Figure 3 (a) and (b) for 2-mm and 1-mm cavity length, respectively. Both co-doped and p-type doped QD lasers maintain the ground-state lasing up to 160 °C and 120 °C for 2-mm and 1-mm cavity lengths, respectively. The n-type doped QD laser exhibits ground-state lasing up to 150 °C for a 2-mm cavity length and dual-state lasing at 110 °C for a 1-mm cavity length. Undoped QD lasers with 2-mm and 1-mm cavity lengths show ground-state lasing up to 145 °C and 110°C, respectively. Notably, for the undoped QD laser, a blue-shift in the peak wavelength was observed at high-temperature ranges. This shift is believed to be caused by a high current injection-induced variation in effective refractive index [34]. In general, a red-shift caused by temperature-induced bandgap shrinkage dominates over the carrier-induced blue-shift, such as band-filling effect and plasma effect, in a moderate temperature range. At high temperature over 100 °C, however, an increased $J_{th}$ and low quantum efficiency result in a large amount of unclamped excess carriers [35], which would be enough to trigger a blue-shift that eclipses the red-shift. For the n-type doped QD laser with a 1-mm cavity length, in addition, a blue-shift at 110 °C was also observed. Its better tolerance to the blue-shift, compared to the undoped QD laser, can be attributed to its lower threshold current density and lower linewidth enhancement factor [36].

It should be noted that, unlike the doped QD lasers, confirming the ground-state lasing of an undoped QD laser in a high-temperature range is challenging due to the blue-shift. In order, therefore, to examine the dual-state lasing often observed prior to the transition to excited-state lasing [37], we measured the injection current-dependent optical spectrum (not shown here). For the undoped QD laser with a 1-mm cavity length, dual-state emission was observed above an injection current of 400-mA at 110 °C, which confirms the excited-state lasing peak of 1257 nm. However, the undoped QD laser with a 2-mm cavity length didn't exhibit the dual-state emission up to our injection current limit.
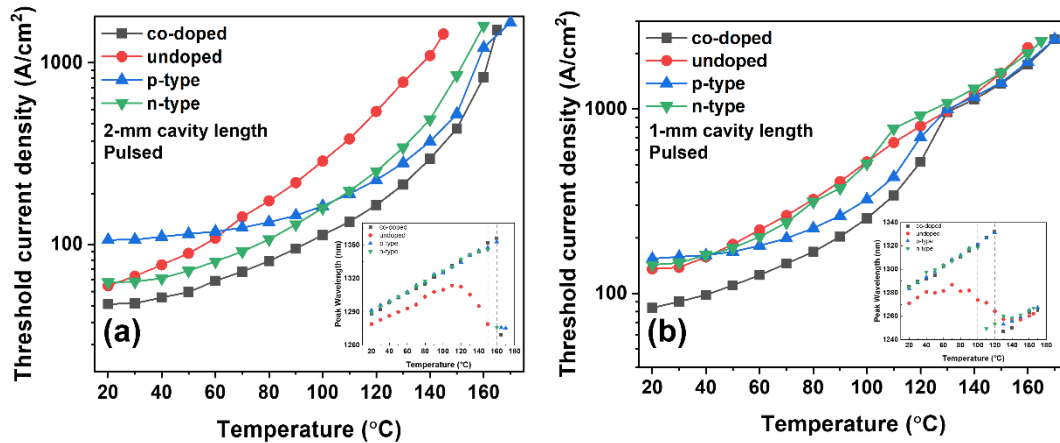


*Figure 3. The temperature dependence of threshold current density for QD lasers with different doping strategies (a) with 2 mm cavity length and (b) with 1 mm cavity length.*

The QD lasers with 2-mm cavity length are also characterised under CW mode, while Figure 4 (a) presents the temperature-dependent $J_{th}$ of four QD lasers. The overall trend of $J_{th}$ under CW mode is similar to that under pulsed injection, but the maximum operating temperature differs depending on the doping strategy. As shown in Figure 4 (a), the co-doped QD lasers produce the lowest $J_{th}$ of 71.69 A/cm$^2$ at room temperature, while the undoped, p-type doped and n-type doped devices show $J_{th}$ of 114.56, 192.96 and 88.56 A/cm$^2$, respectively. It is also observed that the maximum operating temperature of co-doped QD lasers is 115 °C, which is even higher than that of p-type doped QD lasers (105 °C). The temperature-dependent peak lasing wavelength of QD lasers under CW mode, measured at $1.1 \times I_{th}$, confirms ground-state lasing in the inset of Figure 4 (a). The wavelength shifts of co-doped, undoped, p-type doped and n-type doped QD lasers were derived to be 0.55, 0.55, 0.53 and 0.57 nm/K, respectively. Figure 4 (b) shows the light-current-voltage (*LIV*) curve of 2-mm long lasers with different doping strategies under CW mode.
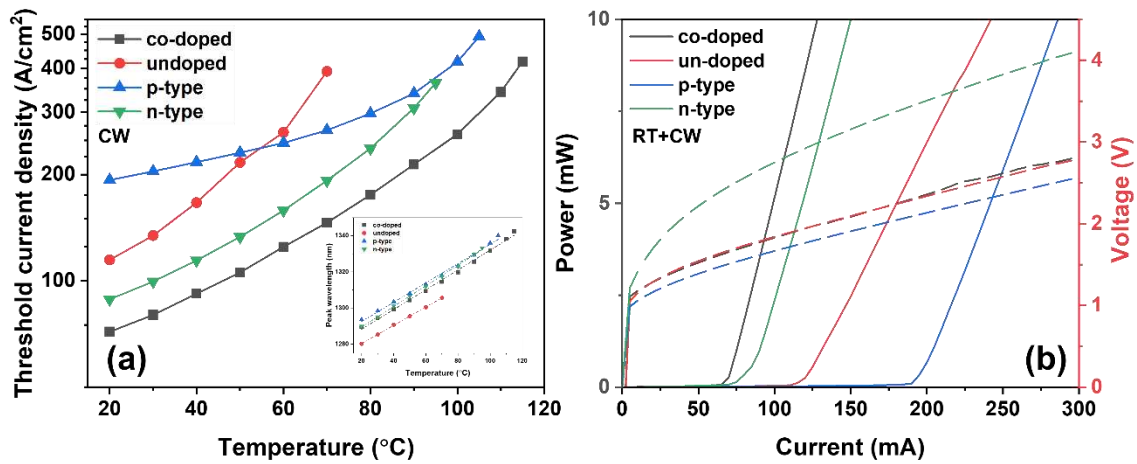
Figure 4. (a) The temperature dependence of CW threshold current density of QD lasers with different doping techniques (2 mm × 50 µm). The inset figure shows the temperature-dependent peak lasing wavelengths of QD lasers. (b) The CW single facet L-I-V curve of 2 mm cavity QD lasers with different doping strategies.

## 4. Simulation

To investigate the observed performance differences in QD lasers that have active regions with various doping strategies, a rate equation model is employed to analyse the effects of dopants. This model simplifies the dynamics of QD lasers by considering four energy levels: the wetting layer (WL), the second and first excited states (ES2 and ES1, respectively), and the ground state (GS).
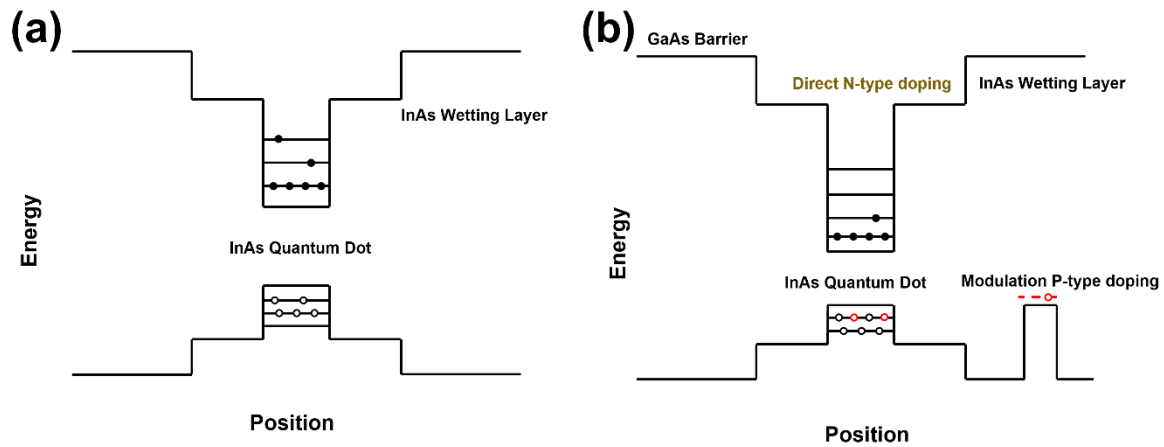


Figure 5. Schematic diagram showing energy levels and singular DWELL layer for (a) an undoped laser and (b) a co-doped laser. Black circles denote the electrons, while white circles and red circles denote the holes and holes from dopants, respectively.

The model operates under a few key assumptions. Firstly, it assumes that the injected current remains constant throughout the operation. Secondly, it posits that relaxation and escape processes occur exclusively between adjacent energy states. Thirdly, the current is considered to be injected directly into the wetting layer (WL). Factors such as the heating effect of the current and variations in QD size are disregarded in this model. To further demonstrate the effect of co-doping technique, the full device band structures are calculated through a semi-empirical model in *Nextnano*. Figure 5 (a) describes a standard band diagram of a single DWELL layer. The effect of the co-doping technique can be divided into two parts: direct n-type doping and modulation p-type doping. During the n-type direct doping, the dopants were directly incorporated into the QD, creating a positive potential as a result of dopants ionising. In addition, the positive ion reduces the number of confined hole states, increasing the

probability of radiative recombination. Meanwhile, for the modulation p-type doping technique, the dopant holes diffuse into the active region shown as a red circle in Figure 5 (b), which also introduce an enhance in radiative recombination.
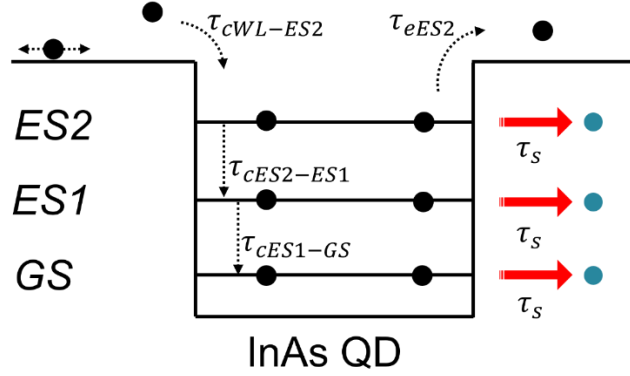


*Figure 6. Schematic diagram showing the electron transitions in the conduction band under rate equation assumptions.*

As depicted in Figure 6, the rate equations governing the system are formulated in equations (1) through (7). These equations collectively provide a framework for understanding the impact of Si doping on QD laser performance, particularly in terms of how the dopants influence the dynamics across the different energy levels.

$$\frac{dN_{WL}}{dt} = \eta_i \frac{I}{q} - \frac{N_{WL}}{\tau_{qr}} - \frac{N_{WL}}{\tau_{cWL-ES2}}(1 - f_{ES2}) + \frac{N_{ES2}}{\tau_{eES2}} \tag{1}$$

$$\frac{dN_{ES2}}{dt} = -\frac{N_{ES2}}{\tau_r} - \Gamma v_g g_{ES2}(2f_{ES2} - 1)S_{ES2} + \frac{N_{ES2}}{\tau_{eES2-ES1}}(1 - f_{ES1}) + \frac{N_{ES1}}{\tau_{eES1}}(1 - f_{ES2}) \tag{2}$$

$$\frac{dN_{ES1}}{dt} = -\frac{N_{ES1}}{\tau_r} - \Gamma v_g g_{ES1}(2f_{ES1} - 1)S_{ES1} + \frac{N_{GS}}{\tau_{eGS}}(1 - f_{ES1}) - \frac{N_{ES1}}{\tau_{cES1-GS}}(1 - f_{GS}) + \frac{N_{ES2}}{\tau_{cES2-ES1}}(1 - f_{ES1}) - \frac{N_{ES1}}{\tau_{eES1}}(1 - f_{ES2}) \tag{3}$$

$$\frac{dN_{GS}}{dt} = -\frac{N_{GS}}{\tau_r} - \Gamma v_g g_{GS}(2f_{GS} - 1)S_{GS} - \frac{N_{GS}}{\tau_{eGS}}(1 - f_{ES1}) + \frac{N_{ES1}}{\tau_{cES1-GS}}(1 - f_{GS}) \tag{4}$$

$$\frac{dS_{ES2}}{dt} = -\frac{S_{ES2}}{\tau_s} + \Gamma v_g g_{ES2}(2f_{ES2} - 1)S_{ES2} + \beta_{sp}\frac{N_{ES2}}{\tau_{sp}} \tag{5}$$

$$\frac{dS_{ES1}}{dt} = -\frac{S_{ES1}}{\tau_s} + \Gamma v_g g_{ES1}(2f_{ES1} - 1)S_{ES1} + \beta_{sp}\frac{N_{ES1}}{\tau_{sp}} \tag{6}$$

$$\frac{dS_{GS}}{dt} = -\frac{S_{GS}}{\tau_s} + \Gamma v_g g_{GS}(2f_{GS} - 1)S_{GS} + \beta_{sp}\frac{N_{GS}}{\tau_{sp}} \tag{7}$$

Photon lifetimes ($\tau_s$) were determined using time-resolved PL measurements, fitted with a mono-exponential function, $I(t) = A \times e^{-t/\tau_s}$. The estimated $\tau_s$ for various lasers at 300 K were 2.43 ns (unintentional doped), 2.36 ns (n-type), 2.59 ns (modulation p-type), and 2.38 ns (co-doped). Other parameters for QD laser components, as shown in Table II, were initially selected from previous simulations and adjusted to replicate experimental L-I curves of InAs QD lasers at 300 K. Simulation results, as shown in Figure 7, strongly suggested that the lifetime of the carriers and the carrier capture within the laser have a significant impact on the threshold current of the laser at room temperature. A shorter carrier lifetime typically leads to a lower threshold current, which is vital for further optimising QD laser design and enhancement.
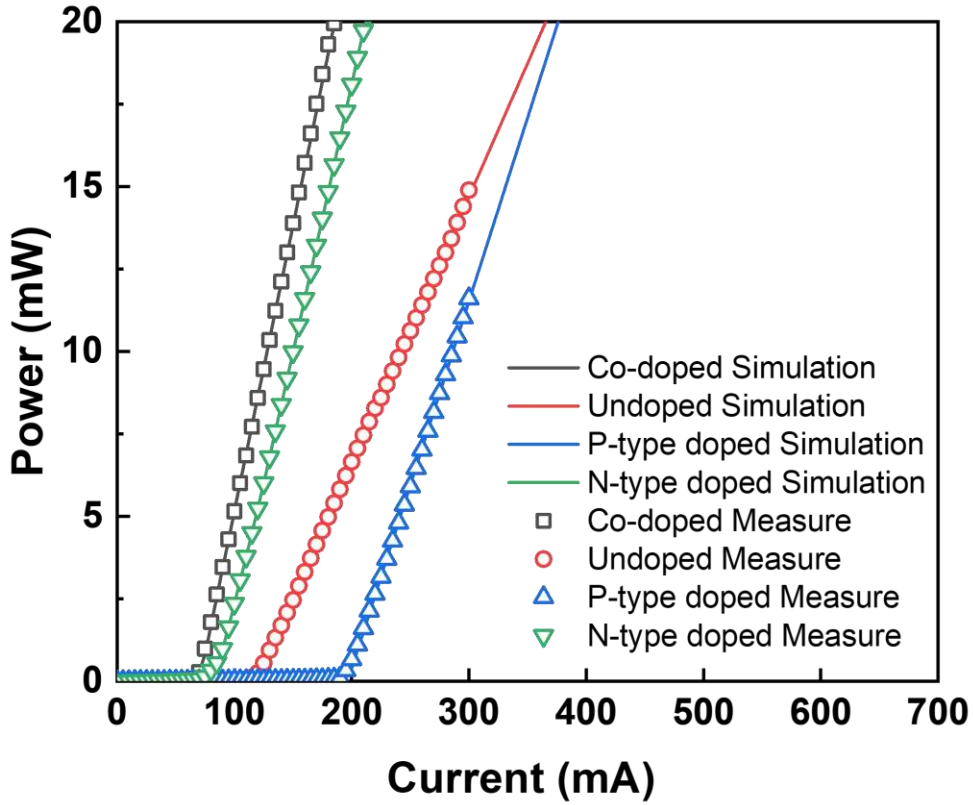
*Figure 7. The comparison of the theoretical simulations and measured results of the InAs QD lasers LI curves with different doping strategies.*

Table II Parameters for rate equation model used for InAs/GaAs QD laser at 300K.

| Symbol | Value |
|---|---|
| Photon lifetimes $\tau_s$ (ns) | 2.43 (undoped), 2.36 (n-type), 2.59 (p-type) and 2.38 (codoped) |
| Capture time from WL to ES2 $\tau_c$ (ps) | 3 (n-type, codoped) / |
| | 8.2 (undoped/ p-type) |
| Relaxation time from ES2 to ES1 $\tau_{ES2\text{-}ES1}$ (fs) | 250 |
| Relaxation time from ES1 to GS $\tau_{ES1\text{-}GS}$ (fs) | 250 |
| QD density $N_D$ (cm$^{-2}$) | $4.5 \times 10^{10}$ |
| Gain in GS $g_{GS}$ (μm$^{-1}$) | $259.38 \times 10^{-4}$ |
| Gain in ES1 $g_{ES1}$ (μm$^{-1}$) | $437.58 \times 10^{-4}$ |
| Gain in GS $g_{ES2}$ (μm$^{-1}$) | $455.30 \times 10^{-4}$ |
| Thermal escape time from GS to ES1 $\tau_{eGS}$ (ps) | 1.6 |
| Thermal escape time from ES1 to ES2 $\tau_{eES1}$ (ps) | 2.1 |
| Thermal escape time from ES2 to WL $\tau_{eES2}$ (ps) | 3.7 |

5. Conclusion

The high-temperature operations of 1.3-μm InAs/GaAs QD lasers with different doping modulations were compared and explained. The performance of 1.3-μm QD lasers was examined with p-type modulation doping, direct n-type doping, co-doping and unintentional doping over a wide temperature range. The results indicate that co-doping significantly reduces the threshold current density, enhancing the high-temperature operational stability of the QD lasers. Notably, while co-doping suppresses ground-state quenching as effectively as p-type doping, it also achieved a much lower threshold compared to p-type doped lasers. In addition, with the help of the rate equation model, we reveal that co-doping optimises the distribution of carriers inside the QDs, which thereby improves the lasers' performance. These findings are especially promising as they suggest that enhanced laser performance can be achieved through a simplified doping approach.

References

1. Kageyama, T., et al., *Extremely high temperature (220°C) continuous-wave operation of 1300-nm-range quantum-dot lasers*, in *2011 Conference on Lasers and Electro-Optics Europe and 12th European Quantum Electronics Conference (CLEO EUROPE/EQEC)*. 2011. p. 1-1.
2. Chen, S.M., et al., *Electrically pumped continuous-wave III-V quantum dot lasers on silicon.* Nature Photonics, 2016. **10**(5): p. 307-+.
3. Jung, D., et al., *Highly Reliable Low-Threshold InAs Quantum Dot Lasers on On-Axis (001) Si with 87% Injection Efficiency.* ACS Photonics, 2017. **5**(3): p. 1094-1100.
4. Duan, J., et al., *Semiconductor quantum dot lasers epitaxially grown on silicon with low linewidth enhancement factor.* Applied Physics Letters, 2018. **112**(25).
5. Duan, J.N., et al., *1.3-μm Reflection Insensitive InAs/GaAs Quantum Dot Lasers Directly Grown on Silicon.* Ieee Photonics Technology Letters, 2019. **31**(5): p. 345-348.
6. Park, J.-S., et al., *Monolithic III–V quantum dot lasers on silicon*, in *Semiconductor Nanodevices*. 2021. p. 353-388.
7. Yadav, A., et al., *Edge emitting mode-locked quantum dot lasers.* Progress in Quantum Electronics, 2023. **87**.
8. Norman, J.C., et al., *A Review of High-Performance Quantum Dot Lasers on Silicon.* Ieee Journal of Quantum Electronics, 2019. **55**(2).
9. He, Y.M., et al., *10-Gbps 20-km Feedback-Resistant Transmission Using Directly Modulated Quantum-Dot Lasers.* Ieee Photonics Technology Letters, 2020. **32**(21): p. 1353-1356.
10. Liu, Z., et al., *Origin of Defect Tolerance in InAs/GaAs Quantum Dot Lasers Grown on Silicon.* Journal of Lightwave Technology, 2020. **38**(2): p. 240-248.
11. Norman, J.C., R.P. Mirin, and J.E. Bowers, *Quantum dot lasers—History and future prospects.* Journal of Vacuum Science & Technology A: Vacuum, Surfaces, and Films, 2021. **39**(2).
12. Tang, M., et al., *Integration of III-V lasers on Si for Si photonics.* Progress in Quantum Electronics, 2019.
13. Zhou, T., et al., *Continuous-wave quantum dot photonic crystal lasers grown on on-axis Si (001).* Nature Communications, 2020. **11**(1): p. 977.

14.     Yang, J., et al., *From past to future: on-chip laser sources for photonic integrated circuits.* Light: Science & Applications, 2023. **12**(1): p. 16.

15.     Benisty, H., C.M. Sotomayortorres, and C. Weisbuch, *Intrinsic Mechanism for the Poor Luminescence Properties of Quantum-Box Systems.* Physical Review B, 1991. **44**(19): p. 10945-10948.

16.     Ukhanov, A.A., et al., *Comparison of the carrier induced refractive index, gain, and linewidth enhancement factor in quantum dot and quantum well lasers.* Applied Physics Letters, 2004. **84**(7): p. 1058-1060.

17.     Bimberg, D., et al., *InGaAs-GaAs quantum-dot lasers.* Ieee Journal of Selected Topics in Quantum Electronics, 1997. **3**(2): p. 196-205.

18.     Jiang, H. and J. Singh, *Strain distribution and electronic spectra of InAs/GaAs self-assembled dots: An eight-band study.* Physical Review B, 1997. **56**(8): p. 4696-4701.

19.     Shchekin, O.B. and D.G. Deppe, *The role of p-type doping and the density of states on the modulation response of quantum dot lasers.* Applied Physics Letters, 2002. **80**(15): p. 2758-2760.

20.     Shchekin, O.B. and D.G. Deppe, *1.3 μm InAs quantum dot laser with To=161 K from 0 to 80 °C.* Applied Physics Letters, 2002. **80**(18): p. 3277-3279.

21.     Yang, J., et al., *All-MBE grown InAs/GaAs quantum dot lasers with thin Ge buffer layer on Si substrates.* Journal of Physics D: Applied Physics, 2020. **54**(3): p. 035103.

22.     Maximov, M.V., et al., *The influence of p-doping on two-state lasing in InAs/InGaAs quantum dot lasers.* Semiconductor Science and Technology, 2013. **28**(10).

23.     Korenev, V.V., et al., *Effect of modulation p-doping level on multi-state lasing in InAs/InGaAs quantum dot lasers having different external loss.* Applied Physics Letters, 2017. **111**(13).

24.     Marko, I.P., et al., *Carrier transport and recombination in p-doped and intrinsic 1.3μm InAs／GaAs quantum-dot lasers.* Applied Physics Letters, 2005. **87**(21).

25.     Alexander, R.R., et al., *Systematic Study of the Effects of Modulation p-Doping on 1.3-$\mu{\hbox {m}}$ Quantum-Dot Lasers.* IEEE Journal of Quantum Electronics, 2007. **43**(12): p. 1129-1139.

26.     Inoue, T., et al., *Impurity doping in self-assembled InAs/GaAs quantum dots by selection of growth steps.* Journal of Applied Physics, 2010. **108**(6).

27.     Kita, T., R. Hasagawa, and T. Inoue, *Suppression of nonradiative recombination process in directly Si-doped InAs/GaAs quantum dots.* Journal of Applied Physics, 2011. **110**(10).

28.     Wang, K.F., et al., *Si delta doping inside InAs/GaAs quantum dots with different doping densities.* Journal of Vacuum Science & Technology B, 2012. **30**(4).

29.     Lv, Z.-R., et al., *Improved performance of 1.3-μm InAs/GaAs quantum dot lasers by direct Si doping.* Applied Physics Letters, 2018. **113**(1).

30.     Deng, H., et al., *The role of different types of dopants in 1.3 μm InAs/GaAs quantum-dot lasers.* Journal of Physics D: Applied Physics, 2022. **55**(21).

31.     Lv, Z.-R., et al., *Significantly improved performances of 1.3 μm InAs/GaAs QD laser by spatially separated dual-doping.* Applied Physics Letters, 2022. **121**(2).

32.     Wang, S., et al., *Significantly enhanced performance of InAs/GaAs quantum dot lasers on Si(001) via spatially separated co-doping.* Optics Express, 2023. **31**(12).

33.     Jarvis, L., et al. *$1.3-\mu\mathrm {m} $ InAs Quantum Dot Lasers with P-type modulation and direct N-type co-doping*. in *2022 28th International Semiconductor Laser Conference (ISLC)*. 2022. IEEE.

34.     Bennett, B.R., R.A. Soref, and J.A. Del Alamo, *Carrier-induced change in refractive index of InP, GaAs and InGaAsP.* IEEE Journal of Quantum Electronics, 1990. **26**(1): p. 113-122.

35.     Murasawa, K., T. Hidaka, and K. Sato, *Injection-current-induced blue-shift laser diode: concept of excess carrier conservation.* Japanese Journal of Applied Physics, 2011. **50**(4R): p. 042101.

36.     Qiu, Y.-Q., et al., *Improved linewidth enhancement factor of 1.3-μm InAs/GaAs quantum dot lasers by direct Si doping.* AIP Advances, 2021. **11**(5).

37.     Maximov, M., et al., *The influence of p-doping on two-state lasing in InAs/InGaAs quantum dot lasers.* Semiconductor science and technology, 2013. **28**(10): p. 105016.